

Morphology evolution of electrodeposited lithium on metal substrates

XingXing Jiao^a, Yongjing Wang^a, Olesya O. Kapitanova^a, Xieyu Xu^a, Valentyn S. Volkov^b, Yangyang Liu^{a,*}, Zhongxiao Song^{a,*}, Aleksandar Matic^c, Shizhao Xiong^{c,*}

^a State Key Laboratory for Mechanical Behavior of Materials, Xi'an Jiaotong University, 28 Xianning West Road, Xi'an, Shaanxi, 710049, China

^b Emerging Technologies Research Center, XPANCEO, Dubai, DIFC, 00000, UAE

^c Department of Physics, Chalmers University of Technology, SE, 412 96, Göteborg, Sweden

ARTICLE INFO

Keywords:
Li metal anode
morphology evolution
electrodeposition
nucleation
microstructures

ABSTRACT

Lithium (Li) metal is deemed to be the high-energy-density anode material for next generation batteries, but its practical application is impeded by the uneven electrodeposition during charge of battery, which leads to the low Coulombic efficiency and potential safety issue. Here, multiscale modeling is fabricated to understand the morphology evolution of Li during electrodeposition process, from the self-diffusion of Li adatoms on electrode surface, to the nucleation process, and to the formation of Li microstructures, revealing the correlation between final morphology and deposition substrates. Energy batteries and self-diffusion of Li adatom on various substrates (lithium, copper, nickel, magnesium, and silver) result in the different nucleation size, which is calculated by kinetic Monte Carlo simulation based on classical nucleation theory. Formation of Li substructures that are grown from Li nuclei, is revealed by phase field modeling coupled with cellular automaton method. Our results show that larger Li nuclei is obtained under faster self-diffusion of Li adatom, leading to the low aspect ratio of Li substructures and the subsequent morphology evolution of electrodeposited Li. Furthermore, the electrodeposition of Li is strongly regulated by the selection of substrates, giving the practical guideline of anode design in rechargeable Li metal batteries. It is worthy to mention that this method to investigate the electro-crystallization process involving nucleation and growth can be transplanted to the other metallic anode, such as sodium, potassium, zinc, magnesium, calcium and the like.

1. Introduction

The past few decades have witnessed the explosive growth of the demand of energy storage along with the required sustainability of energy in society [1], especially in the electrification of automotive industry [2]. However, lithium-ion batteries (LIBs), the state-of-the-art energy storage technology, have nearly approached their limit of energy density, around 300 Wh·kg⁻¹, which is rooted in the theoretical specific capacity of the cathode material and the graphite anode (372 mAh g⁻¹) [3,4]. Lithium (Li) metal, has an ultrahigh specific theoretical capacity of 3860 mAh·g⁻¹ and the lowest reduction potential of -3.04 V (versus standard hydrogen electrode) [5], promising a high energy density when coupled with high capacity cathode materials in new battery chemistries like Li-sulfur (2600 Wh·kg⁻¹) and Li-oxygen (3500 Wh·kg⁻¹) [6]. Thus, replacing the commercial graphite anode with Li metal anode is seemingly a straightforward approach to realize energy storage systems

beyond LIBs [7,8]. Nevertheless, the utilization of Li metal as anode in rechargeable batteries is hindered by low Coulombic efficiency, short cycle life as well as the safety issues, which are mainly a result of nonuniform electrodeposition during cycling and the instability against the electrolyte [9,10].

Indeed, the nonuniform electrodeposition of Li is attributed to the mismatch between the sluggish mass-transfer of Li-ions near the electrode and fast charge-transfer kinetic of the electrochemical reaction, $\text{Li}^+ + e^- \rightarrow \text{Li}$, forming mossy and dendritic Li microstructures rather than dense metal [11–14]. The growth of dendritic Li with large surface area will exacerbate side-reactions with the electrolyte forming solid electrolyte interphase (SEI) film over all surfaces in the electrode. Commonly the SEI film is fragile and easily broken by interfacial displacement during cycling, triggering even more side reactions. This leads to continuous consumption of active Li metal as well as electrolyte, lowering Coulombic efficiency and cycle life of the cell. Moreover, the

* Corresponding author.

E-mail addresses: liuyy123@stu.xjtu.edu.cn (Y. Liu), zhongxiao.song@mail.xjtu.edu.cn (Z. Song), matic@chalmers.se (A. Matic), shizhao.xiong@chalmers.se (S. Xiong).

accumulation of side reaction products also increases the interfacial resistance and results capacity decay. To regulate Li electrodeposition, a plethora of strategies have been developed targeting the key mechanisms for dendrite formation, such as accelerating mass-transfer and slowing down charge-transfer kinetics. These strategies can be sorted into: (i) building an artificial SEI on Li [15–18], (ii) optimizing electrolytes in terms of solvents and Li salts [19–22], (iii) structural design of composite Li anodes [23,24], and (iv) introducing solid-state electrolytes [25–28]. However, the requirement on Coulombic efficiency of a Li-metal anode in practical battery systems, above 99.9%, has yet to be achieved, hindered by a lack of a mechanistic understanding of the electrochemical deposition processes of Li, from the initial state to the final morphology where the morphology develops from nm to μm length scales [29–31].

Electrocrystallization of Li on the electrode surface is closely linked to the properties of substrate, which impact the reduction of Li-ions, the self-diffusion of Li adatoms on the substrate surface, and the formation of Li nuclei [32–36]. In particular, lithophilicity of the substrate has been recognized as an important parameter to tune the electrocrystallization of Li metal at the initial stage of electrodeposition [37, 38]. However, the actual role of the surface property on electrocrystallization of Li and its link to the final morphology is not well understood. Bulk lithium metal has a body-center-cubic (BCC) crystal structure, and the general steps for crystallization can also be applied for the electrodeposition process. Typically, the process can be divided in (i) the self-diffusion of Li adatoms on the surface of the substrate, (ii) the formation of Li nuclei from aggregated Li adatoms or Li embryo, (iii) the growth of Li substructures from nuclei of critical size and (iv) further growth of Li on these substructures. To understand these processes, considerable efforts have been devoted to reveal the influence of a certain step by using simulation methods like density function theory (DFT), finite elements analysis, and cellular automaton simulations [35, 39,40]. However, linking the initial electrocrystallization process of Li on a substrate to the microstructures found at end of electrodeposition needs an overall understanding from the self-diffusion to the growth of deposited Li, involving multiple length scales.

Herein, we selected typical metal substrates for Li deposition, lithium (Li), copper (Cu), nickel (Ni), magnesium (Mg) [41] and silver (Ag) [37], to investigate correlation between electrocrystallization of Li and the final morphology of deposited Li. A package of simulation tools, DFT, kinetic Monte Carlo based on the classical nucleation theory (CNT), and phase field modeling, were employed to reveal the self-diffusion barriers of Li adatoms, to follow the nucleation process of Li as well as the growth of Li structures, respectively. Our simulations show the capability to continuously track the key steps of electrocrystallization at relevant length scales and to correlate the self-diffusion of Li to the morphology for electrodeposited Li-metal. We find that the lower the self-diffusion barrier is, the larger the critical size of nuclei, subsequently generating Li substructures with low aspect ratio and ultimately resulting in

uniform electrodeposition. Our work not only explores the understanding of the electrocrystallization processes of Li by multiscale modeling, but also provides a guideline to design of the substrate surface for long-life and safe rechargeable Li-metal batteries.

2. Theory and model

2.1. Reduction of Li-ion

As shown in Fig. 1, prior to the electrocrystallization of Li, the overall reaction of $\text{Li}^+ + e^- = \text{Li}$ can be divided into two steps, mass-transfer of desolvated Li-ions to the substrate and charge-transfer to form Li adatoms on the substrate. The mass-transfer process can be described by Fick's law: [14]

$$\frac{\partial C_{\text{Li}^+}(x, t)}{\partial t} = D_{\text{Li}^+} \frac{\partial^2 C_{\text{Li}^+}(x, t)}{\partial x^2}, \quad (1)$$

where $C_{\text{Li}^+}(x, t)$ is the concentration of Li-ions at a certain position (x) above the surface and a certain time (t), D_{Li^+} is the diffusion coefficient of Li^+ in the electrolyte. The charge-transfer kinetics for reduction of Li^+ to form Li adatoms can be described by the Butler-Volmer equation: [42–44]

$$J = j^0 \left[\exp\left(\frac{\alpha F}{RT}\eta\right) - \exp\left(-\frac{\beta F}{RT}\eta\right) \right], \quad (2)$$

where j^0 is the exchange current density, η is the overpotential on the substrate surface, α and β are the transfer coefficients of anodic and cathodic currents ($\alpha + \beta = 1$ for single electron reaction), respectively, F is Faraday constant, R is ideal gas constant and T is the temperature.

2.2. Self-diffusion of Li adatoms on electrode

After the reduction of Li-ions, the generated Li adatoms will be adsorbed on the substrate and move to the suitable spots for electrocrystallization through self-diffusion (Fig. 1). The self-diffusion can be considered as a hopping process, moving between adjacent adsorption sites [45]. For a thermally activated diffusion process the hopping rate of an adatom on a periodic substrate can be expressed through transition state theory: [46]

$$\nu = \frac{\kappa_B T}{h} \exp\left(\frac{-\Delta F}{\kappa_B T}\right), \quad (3)$$

where ΔF is the Helmholtz free energy barrier for hopping between sites in the lattice. κ_B and h are the Boltzmann constant and Planck's constant, respectively. Only nearest-neighbor hopping is considered and the self-diffusion coefficient on the substrate (D_s) is given by the hopping rate ν and hopping distance a by the relation: [47,48]

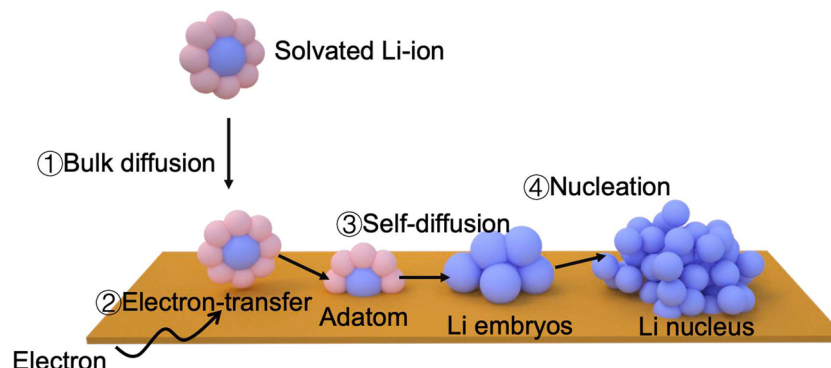


Fig. 1. Schematic diagram of nucleation of Li during electrocrystallization. The process contains mass transfer of Li-ions from bulk electrolyte, reduction of Li-ions to Li atoms, self-diffusion of Li adatoms, formation of Li embryos and nuclei of critical size.

$$D_s = \frac{\nu a^2}{2}. \quad (4)$$

For self-diffusion of Li adatoms on a substrate (Figure S1a), the dynamic equilibrium between the adsorption and dissolution of Li adatoms can be described as:

$$D_s \frac{\partial^2 C_{Li}}{\partial t^2} = \frac{i(x)}{nF}, \quad (5)$$

where C_{Li} is the surface concentration of Li adatoms. According to the Butler-Volmer equation, $i(x)$ is given by:

$$i(x) = j^0 \left[\left(\frac{C_{Li}}{C_{Li}^0} \right) \exp\left(\frac{\alpha F}{RT} \eta\right) - \exp\left(-\frac{\beta F}{RT} \eta\right) \right]. \quad (6)$$

with the boundary conditions:

$$\begin{cases} \lim_{(x,t) \rightarrow (0,0)} C_{Li}(x,t) = C_{Li}^0 \\ \frac{dC_{Li}}{dx} \Big|_{x=x_0} = 0 \end{cases},$$

The surface concentration of Li adatoms is obtained after solving Eq. (5),

$$\frac{C_{Li}}{C_{Li}^0} = \exp\left(\frac{\alpha F}{RT} \eta\right) + \left[1 - \exp\left(\frac{\alpha F}{RT} \eta\right) \right] \frac{\exp\left(-\frac{x}{\lambda_0}\right) \cdot [1 + \exp\left(-\frac{2(x_0-x)}{\lambda_0}\right)]}{[1 + \exp\left(\frac{2x_0}{\lambda_0}\right)]}, \quad (7)$$

where

$$\lambda_0 = \sqrt{\frac{FD_s C_{Li}^0}{j^0} \exp\left(\frac{\beta F \eta}{2RT}\right)}, \quad (8)$$

is regarded as the self-diffusion distance of a Li adatom.

In this work, the self-diffusion process of Li adatoms was modelled with the Vienna Ab-initio Simulation Package (VASP) to obtain the diffusion barriers and hopping rates on different surfaces. The self-diffusion coefficient was then introduced into the simulation of nucleation using kinetic Monte Carlo method, see more details in supplementary information, Step I: Self-diffusion of Li adatom on electrode surface.

2.3. Nucleation of Li clusters

Clusters of Li adatoms larger than a critical size will grow up to form crystal nuclei following the Classical Nucleation Theory (CNT). Here, an hemisphere with radius of r is used to describe a Li nucleus on a substrate and the Gibbs free energy change for formation of this nucleus is defined by the surface energy change $\Delta G_S = \gamma A$ and the bulk energy change $\Delta G_B = -N|\Delta\mu|$ as (Figure S1b): [49]

$$\Delta G(N) = -N|\Delta\mu| + \gamma A \quad (9)$$

where N is the number of atoms in the crystal cluster, $|\Delta\mu| = e\eta$ is the chemical potential difference for the single-electron electroreduction of Li [47], γ is the surface energy and A is the surface area of the cluster. The spontaneous growth of a cluster is determined by the competition between lowering the bulk free energy and increasing the surface energy with increasing cluster the free energy barrier for spontaneous growth and the critical nucleus size N^* can be determined from Eq. (9) giving

$$N^* = \frac{32\pi r^3}{3\rho_s^2(e\eta)^3}, \quad (10)$$

as the critical nucleus size and

$$\Delta G(N^*) = \frac{e\eta N^*}{2}, \quad (11)$$

as the free energy barrier for nucleation, where ρ_s is the number density of a bulk Li and e is the charge per ion. For a semispherical Li nucleus, the critical radius is given by

$$R = \frac{2\gamma}{\rho_s e\eta}, \quad (12)$$

The probability for forming a Li nucleus with size n can be approximated by [50–52]

$$P(n) = \frac{M_n}{M} = \exp\left(\frac{-\Delta G(n)}{\kappa_B T}\right), \quad (13)$$

where M_n is the number of Li nuclei with size n in a system containing Li adatoms with total number of M . Thus, the probability to form a critical nucleus is given by [53]

$$P^* = \exp\left(\frac{-\Delta G(N^*)}{\kappa_B T}\right), \quad (14)$$

To follow the nucleation step lithium clusters with homogeneous size are randomly introduced into the model as cells for the Monte Carlo algorithm at the beginning of the simulation. Based on the diffusion barriers and hopping rates of Li adatoms on different substrates, we can follow the evolution of initial Li clusters during the electrodeposition (with an applied constant current density) and obtain the critical nucleation radius by using the principle of probability statistics, see more details in supplementary information, Step II: Nucleation process of Li.

2.4. Formation and growth of Li microstructures

The simulation of the subsequent evolution of the formed crystal nuclei after electrocrystallization can be divided into two parts, the formation of Li substructures based on the growth of Li nuclei and the further deposition of Li on these Li substructures. The former part is modelled by a combination of cellular automaton simulation in MATLAB and finite element simulations using COMSOL Multiphysics. For the latter part, the simulation of the growth of Li substructures and formation of the final morphology of deposited Li is conducted by phase-field modeling using COMSOL Multiphysics.

3. Results and discussion

First, the energy barriers for hopping of Li adatoms between equilibrium sites the different surfaces were calculated using DFT within the generalized gradient approximation (GGA) to account for exchange correlation effects [54,55]. In a typical diffusion process, the adatom moves from the most favorable adsorption site to a neighboring site and the energy difference between the minimum and maximum energy over this trajectory defines the activation energy for hopping self-diffusion [56]. We calculated the diffusion energy barrier of a single Li adatom on the different substrate surfaces including metallic Li, Cu and Ni that are common current collectors for anodes [57,58], as well as the lithophilic Mg and Ag surface (Figure S2), which have been reported to be interface modifying layers for anode [41,59]. All calculations were conducted on the lowest-energy planes of related surfaces corresponding to Li(100), Cu(111), Ni(111), LiMg(110) and LiAg(110), respectively. In terms to Cu, (111) surface embraces the lowest surface energy of 1.39 J m⁻², which is much lower than that of (100) of 1.47 J m⁻² [60]. Due to the equivalent energy of all sites on the body-centered cubic (BCC) Li (100) surface [61], the energy profile of a diffusing Li adatom is almost symmetric (Figure S3a). In contrast, the diffusion pathways on the face-centered cubic (FCC) surfaces of Cu(111) and Ni(111) are derived from FCC sites and hexagonal-close-packing (HCP) sites [62], showing

the similar energy barrier for Li adatom diffusion on Cu and Ni surfaces, as seen in **Figures S3b-c**. The energy profile of the trajectories on the BCC surfaces of LiMg(110) and LiAg(110) are asymmetric, a result of the very different chemical environments between hopping sites (see the insert of **Figures S3d-e**).

The energy barriers for self-diffusion can be determined from the energy evolution over during a jump from one site to another and are shown in **Figure S3f**. On the Li(100) surface, the hopping of Li adatoms shows the highest barriers and lowest hopping rate, which demonstrates that Li adatoms are almost immobile on an existing crystalline surface and prefer to stick where they are adsorbed and form local protuberances. The energy barriers on Cu(111), Ni(111) and LiMg(110) surfaces are considerably lower the hopping rates higher, illustrating an accelerated self-diffusion of Li adatoms. The LiAg(110) surface shows the lowest barrier and a very high hopping rate. This shows that using lithophilic elements like Mg, Ag to modify the surface for Li electrodeposition accelerates the self-diffusion of Li adatom in the initial stage of electrodeposition. Furthermore, these rates can be introduced into the subsequent modeling of the nucleation process with cellular automaton simulation, which is the state-of-the-art method to simulate growth processes on surfaces with a mesoscopic length scale beyond atomic scale of DFT calculation.

The energy barrier when clusters of Li adatoms reach the critical size is hard to overcome when sampling nucleation events using traditional DFT calculations or molecular dynamics simulations are conducted [63]. Even with advanced sampling techniques, like umbrella sampling [64] or metadynamics sampling with biased potentials [65], the direct nucleation kinetics cannot be unambiguously determined. Here, we instead use kinetic Monte Carlo simulations to simulate the nucleation of Li metal on different surfaces and the self-diffusion of Li adatoms can be regarded as the bridge connecting the atomistic scale of DFT calculations with the nucleation process [52,66]. Our method is based on the relationship between Gibbs free energy change and nucleation size in classical nucleation theory (**Figure S1b**) [63,67] and a pre-existing cluster of Li adatoms is introduced as embryo for further nucleation. Critical nucleation of Li can be considered as an event that embeds a larger

crystal cluster or embryo on a surface and we monitor the growth or dissolution of the embryo. Thus, the pre-existing embryo are far smaller than critical size of Li nucleus created in the kinetic Monte Carlo simulation [68]. During Monte Carlo simulation, the growth of Li embryos stem from the self-diffusion of Li adatoms and the process is conducted by 1000 times to observe the probability of stable Li nuclei with certain sizes [69].

Taking the nucleation process on the native Li surface as example, the distribution of nucleus radii is centered at 52 nm with a confidence probability (CP) of 10%, which means that nuclei with this radius will most likely be dissolved, whereas a nucleus of 98 nm with a CP=90% has a large chance to grow (**Fig. 2b**). With the increase of CP from 10% to 90%, the distribution of radii narrows gradually, which indicates that the formation of Li nuclei with the centered radius is more probable. When Li nucleates on surfaces with lower diffusion energy barriers (Cu and Ni), the size of nuclei is larger and with a broader distribution than that on the Li surface. There is a very small difference in the distributions, position and width, for Li nuclei on Cu and Ni surfaces, illustrating that the nucleation of Li metal on these surfaces is quite similar (**Fig. 2c-d**). The lithophilic surfaces (LiMg or LiAg) show wider distributions (**Fig. 2e-f**) and the LiAg surface shows the largest nucleation size, >250 nm, at high confidence probability but also a wider distribution (**Fig. 2f**).

The dependence of Li nuclei radius on CP derived from the kinetic Monte Carlo simulations is plotted in **Fig. 3a**. The radius obviously increases with the increasing CP. Overall the radius is the smallest on the surface of Li which has the highest energy barrier for self-diffusion. The sizes of Li nuclei on Cu and Ni are almost the same, in agreement with the similar energy barriers of self-diffusion. Interestingly, Li nuclei have also a smaller size on the LiAg surface at the beginning of simulation (CP=10%), illustrating that the low energy barrier for self-diffusion of Li adatoms enables great availability for the free diffusion. However, the size of Li nuclei on LiAg surface turns to be the largest one CP is > 10% as the simulation proceeds. Thus, both the initial nucleation and the following process are controlled by the energy barrier for self-diffusion of Li adatoms on the substrate surface. For the final state of simulation, the size of Li nuclei reaches the critical threshold with CP=100% and

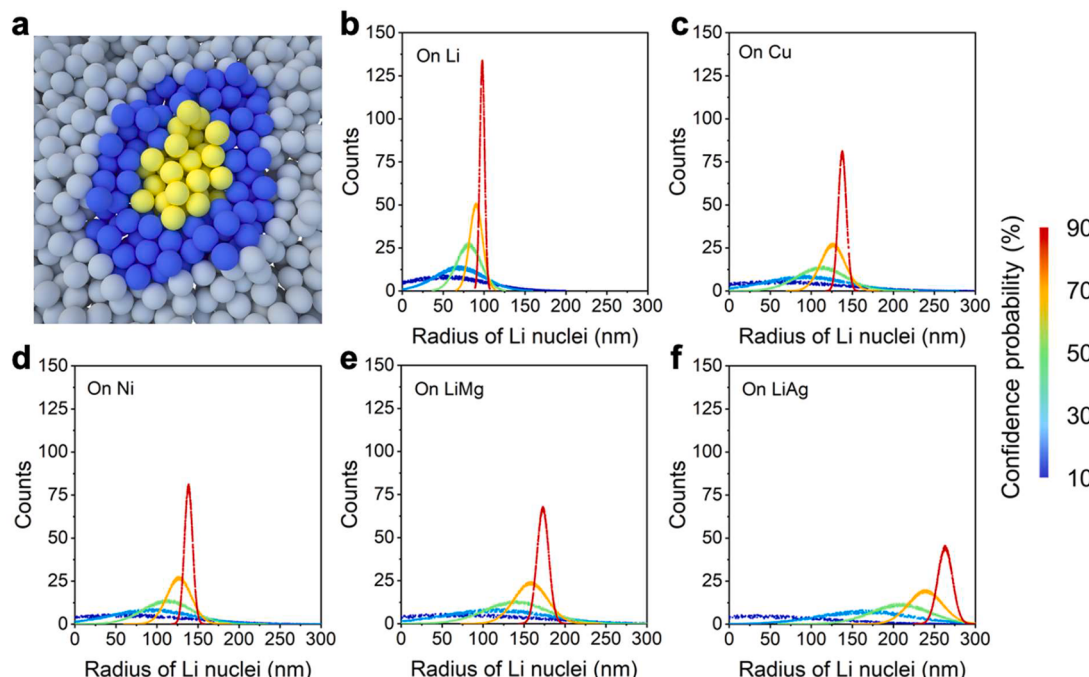


Fig. 2. Nucleation process of Li on different surfaces with a Li adatom embryo. (a) Schematic diagram for nucleation of Li. Gray balls represent Li ions in the system. Blue balls represent the Li atoms reduced from ions or dissolved from nucleus. Yellow balls represent Li atoms in stable nucleus. Radius of Li nuclei on the surface of (b) Li, (c) Cu, (d) Ni, (e) LiMg and (f) LiAg with a series of confidence probability (CP) during Monte Carlo simulation.

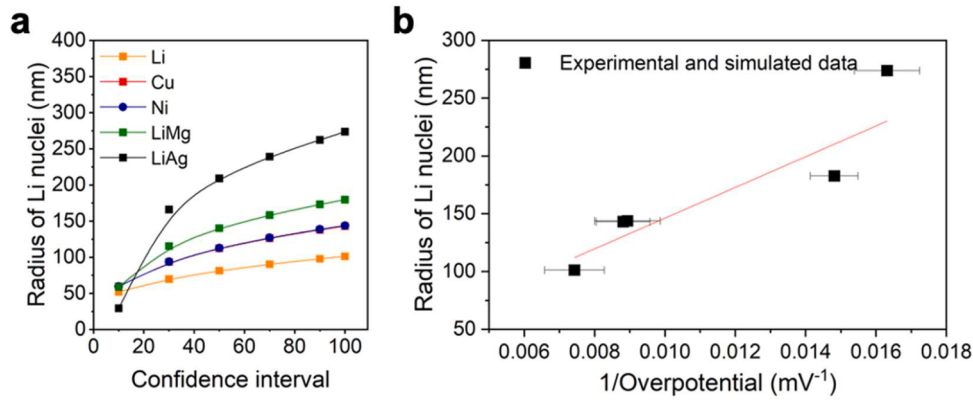


Fig. 3. Distribution of radius of Li nuclei on different surfaces. (a) Radius of Li nuclei as a function of confidence probability. (b) Relationship between the simulated critical radius of Li nuclei and experimentally determined nucleation overpotential.

this means that the cluster is thermodynamically stable.

According to the Eq. (12) the critical radius of Li nuclei is inversely proportional to the nucleation overpotential [53]. To test this relation, the overpotentials for nucleation of Li on different substrates, including Li disk, Cu disk, Ni disk, Mg coated Cu disk and Ag coated Cu disk, were experimentally determined from the voltage profiles shown in Figure S4. The scanning electron microscopy (SEM) has been conducted to detected the nuclei of Li metal on different surface at current density of 0.5 mA cm⁻². As shown in Figure S5, the Li nuclei show the spherical shape at the beginning of electrodeposition process, the associated diameters are about 100 nm on Li surface, 150 nm on Cu surface, 180 nm on LiMg surface and 250 nm on LiAg surface respectively, which are consistent with the simulation results. From Fig. 3b it is clear that the correlation between the experimentally determined overpotential for nucleation and the simulated critical size of the nuclei follows the suggested relation in eq. 16, demonstrating the validity of the approach using the kinetic Monte Carlo method.

In our work, the growth of Li nuclei to the final morphology is divided into two steps, formation of Li substructures and growth of these to the final morphology, occurring on submicron to micron scales. For the formation of Li substructures, the generated Li nuclei are assumed to be thermodynamically stable after their size reaches the critical value. Then the formation of Li substructures is simulated by the cellular automaton method, linked to phase-field modeling with a Python script [70]. At the initial stage of simulation, the Li substructures grow at a relatively low rate on the LiAg surface, which is attributed to the fast self-diffusion of Li adatoms (Figure 4a_i and Figure S6a_i). The growth rate is accelerated, and higher electrodeposited structures are formed when

the self-diffusion is slower, i.e. on the surfaces of LiMg, Ni/Cu, and Li (Figure 4b_i, c_i, d_i and Figure S6b_i, c_i, d_i). As the electrodeposition proceeds, the Li substructures on the LiAg surface are relatively dense and short, as shown in Figure 4a_i and S6a_i. By comparison, the Li substructures on the substrates with more sluggish self-diffusion show a more porous structure and the porosity increases with lower self-diffusion (Fig. 4b-d and S6b-d). It is worth noting that the final morphology of Li substructures on Li substrate shows a branched structure, as a result of the surface having a high barrier for self-diffusion.

The current density on the top of higher Li substructures is enhanced, Fig. 4b-d. As shown in Figure S7, both the maximum of Faradic current density and the difference between top and bottom regions of the substructures are higher on substrates with slow self-diffusion of Li adatoms. The enhanced Faradic current density will act as a hot spot for further electrodeposition, resulting in rapid growth and also the creation of branched substructures with high porosity. In contrast, the relatively uniform distribution of Faradic current density on Li substructures formed on the LiAg substrate provides the conditions for even electrodeposition of Li in the subsequent step. It suggests that the shape of Li substructures is strongly related to the nucleation process and plays a critical role for the subsequent growth of Li to form the final morphology.

The electrodeposition process corresponding to the growth of Li substructures to the final morphology of Li is simulated by phase-field modeling under a constant current density of 0.5 mA cm⁻². The Li substructures on the different substrates can be characterized by their aspect ratio, Figure S8. The aspect ratio varies from 0.55 on the surface

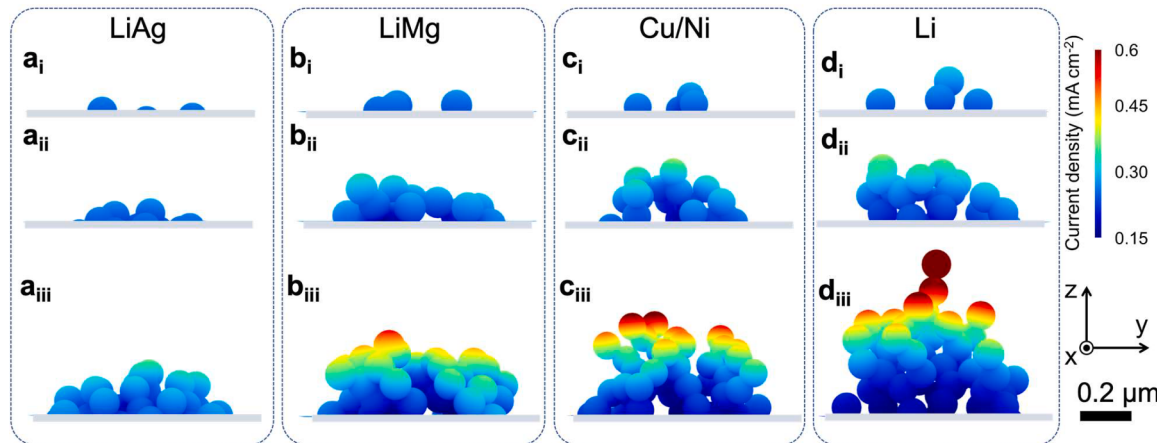


Fig. 4. Li substructures based on growth of Li nuclei on different surfaces. Evolution of Li substructures at (a_i-a_{iii}) LiAg, (b_i-b_{iii}) LiMg, (c_i-c_{iii}) Cu or Ni and (d_i-d_{iii}) Li substrates. i, ii, iii correspond to subsequent steps in the calculation.

of LiAg to 1.78 on surface of Li. This aspect ratio of Li substructure is introduced in the phase field modeling as pillars on the substrate, see details in Figure S9 and Table S1. At the initial stage, the distribution of Li-ion concentration is relatively uniform around the substructures with low aspect ratio, but the uniformity decreases with increasing aspect ratio (Fig. 5a-d). The concentration field can be divided into two regions, the region between two substructures, and the region from the top of a substructure to the bulk electrolyte. As shown in Fig. 5k, the concentration gradient of Li-ion in both regions increases with the aspect ratio. The behavior of the corresponding Faradic current density, Figure S10, directly follows the Li-ion concentration distribution, with an increasing difference of Faradic current density in the taller substructures. These distributions of concentration field and Faradic current density remain throughout the simulation until the convergence stage is reached, Figures S11-S13, and directly contribute to the evolution towards the final morphologies of electrodeposited Li on the different substrates.

The evolution of the electrodeposition probability, and the corresponding morphology, on the substructures with different aspect ratio are shown in Fig. 5e-h. For the substructures with low aspect ratio, as on the LiAg substrate, there is a preferential deposition on the sides of the structures. Thus, the gap between the structures will be filled creating a dense morphology. When the aspect ratio increases

preferentially occurs at the top corners of the substructure and difference of electrodeposition probability between top and bottom is enhanced (Fig. 5f and g). For the Li substrate that has the highest aspect ratio, electrodeposition preferentially occurs on the top generating a bulb-like final morphology (Fig. 5h). The uneven probability for Li electrodeposition will enhance the growth of Li on top of the substructures, which can be a trigger for rapid growth of dendritic Li at this hot spot. To further demonstrate the correlation between aspect ratios and final morphology, the range of aspect ratios was extended up to 4, and the results are shown in Figures S14-S15. As expected, the concentration gradient of Li-ions near the electrode is enhanced and depletion effect for Li-ions is induced by mass-transfer limitations in the electrolyte (Figures S13a-f), promoting non-uniform electrodeposition, see Figures S13g-i. To characterize the electrodeposition, a uniformity factor can be defined as the rate of electrodeposition on the top of the substructures, see inset in Fig. 5l. The uniformity factor reveals an almost linear correlation with initial aspect ratio of substructures, directly reflecting that a denser morphology of electrodeposited Li can be expected with lower initial aspect ratio and a porous Li morphology will be obtained on taller initial Li substructures.

To understand the correlation between the final morphology and the size of the initial Li nuclei in a large scale, a model with an area of 10 μm^2

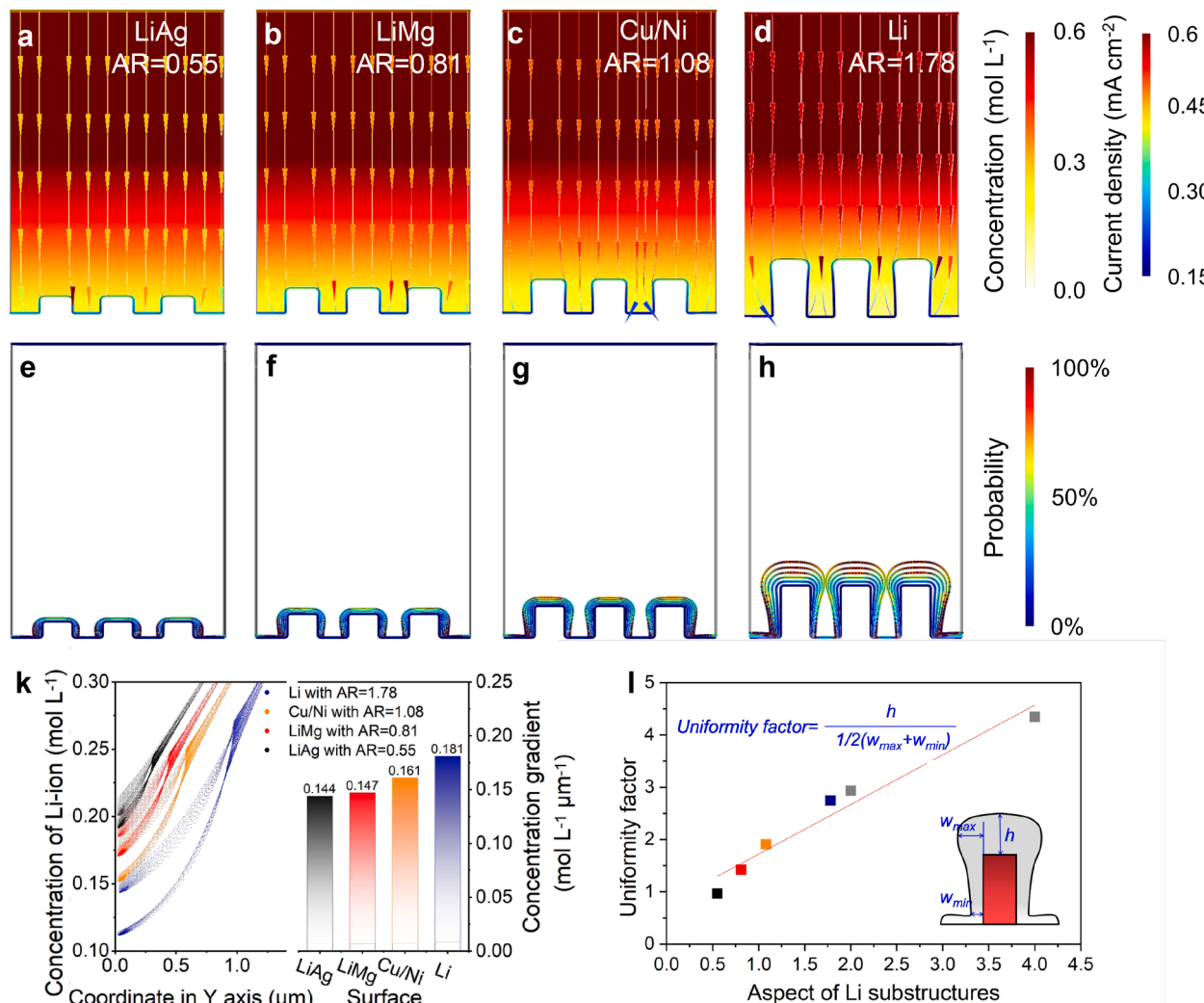


Fig. 5. Growth of substructures to final morphology of electrodeposited Li on different substrates. Concentration field (background color) coupled with electric field (colored lines) near the pillars that act as models for Li substructures on the surface of (a) LiAg, (b) LiMg, (c) Cu/Ni and (d) Li at initial stage (AR=aspect ratio). Evolution of morphology of electrodeposited Li morphology and the electrodeposition probability (colored profile lines) of substructures on the surface of (e) LiAg, (f) LiMg, (g) Cu/Ni and (h) Li. (k) Concentration distribution of Li-ion near the pillar features at initial calculating stage. (l) Uniformity factor deposition on substructures as a function of aspect ratio.

by 10 μm on the deposited Li is constructed to evaluate the morphology evolution under a certain initial roughness. Different structural fluctuation appears on the surface of electrodeposited Li, which is represented by the arithmetic mean deviation (Ra) of surface roughness. Here, a series of Ra values as 0.38, 0.56, 0.57 and 0.95 are generated by a random function to simulate the substructures of electrodeposited Li on metal substrates shown in Fig. 4 and Figure S16. During the electrodeposition process, concentration observed at the high plateau of surface is greater than that at low-lying area, as seen in Figure S16a. With the decreasing of roughness from $\text{Ra}=0.95$ to 0.38, the concentration difference between plateau and lower area turns to be negligible (Figures S16b-d). Hence, uniform concentration can be realized on the low-roughness surface from the development of larger Li nuclei, which is confirmed by the narrow statistics distribution of Li-ion concentration (Figure S16e). The similar trend is obtained for the distribution of current density and higher current density is present on at the high plateau of electrodeposited surface, showing a remarkable difference towards the current density at the low-lying area (Fig. 6a-d). Furthermore, the difference is significantly mitigated with the lowering of roughness and the statistic of current density reveals a more uniform distribution on the substrate with lower roughness, which is resulted from larger Li nuclei (Figs. 6e). The extraction of current density along $y = 5 \mu\text{m}$ and $x = 5 \mu\text{m}$ shows that the variation of current density on the surface with higher roughness, Li, Cu or Ni and LiMg is greater than that on the LiAg surface with lowest roughness (Fig. 6f and g). This is further demonstrated by the declined dispersion coefficient of current density along X and Y axis (Figure S16-17). Both distribution of Li-ion concentration and current density on the surface indicate that the electrodeposition of Li metal is preferred to occur at the high plateau of surface. As a consequence, the roughness of surface increases with the ongoing electrodeposition, and the increasing rate is determined by the initial roughness of Li substructure on different substrates. After electrodeposition of 1.5 mAh Li, a roughness increase of 9.59%, 2.3%, 1.15% and 0.56% is obtained for electrodeposited Li on Li, Cu or Ni, LiMg and LiAg, respectively (Fig. 6h). Experimentally, the cycled Li metal anode that disassembled from Li|Cu

half-cell with Ag and Mg modified Cu current collector shows relative plate and dense morphology, which are much improved compared with the catastrophic dendritic morphology on bare Cu and Ni substrates (Figure S18). Based on this regulation of nucleation of Li metal, the Coulombic efficiency of Li metal anode on Ag modified Cu current collector is greater about 99% at current density of 0.5 mA cm^{-2} , which can hold stable within 140 cycles (Figure S19). Therefore, the final morphology of electrodeposited Li on metal substrates is dependent on the size of the initial Li nuclei, which is related to the self-diffusion of Li adatoms on the surface.

4. Conclusions

In this work, multi-scale modeling was applied to uncover the electrodeposition behavior of Li metal on different substrates, and the Li plating process was investigated in four successive steps: i) self-diffusion of Li adatoms on the substrate, ii) nucleation, iii) formation of Li substructures and iv) growth to the final morphology. DFT calculations of the self-diffusion of Li adatoms show that on lithiophilic surfaces, e.g. LiAg, a high hopping rate and low energy barrier are found, whereas on the native Li-metal surface the self-diffusion of Li adatoms is slow. Introducing these self-diffusion parameters to kinetic Monte Carlo simulations based on the classical nucleation theory enables us to determine the critical nucleation size on the different substrates. Our results reveal a direct correlation between the self-diffusion of Li adatoms and the critical size of Li nuclei, with larger critical nuclei on substrates with high self-diffusion. Subsequently, the cellular automaton method coupled with phase-field modeling reveals the growth of Li substructures with low aspect ratio based on the larger Li nuclei, found on the lithiophilic LiAg substrate. The shape of Li substructures is critical for the final morphology of electrodeposited Li. Substructures with low aspect ratios will have a rather uniform probability for electrodeposition promoting growth to a dense morphology. By coupling the different simulation methods to follow process from atomistic to micrometer scales enables us to show that self-diffusion of Li adatoms on the

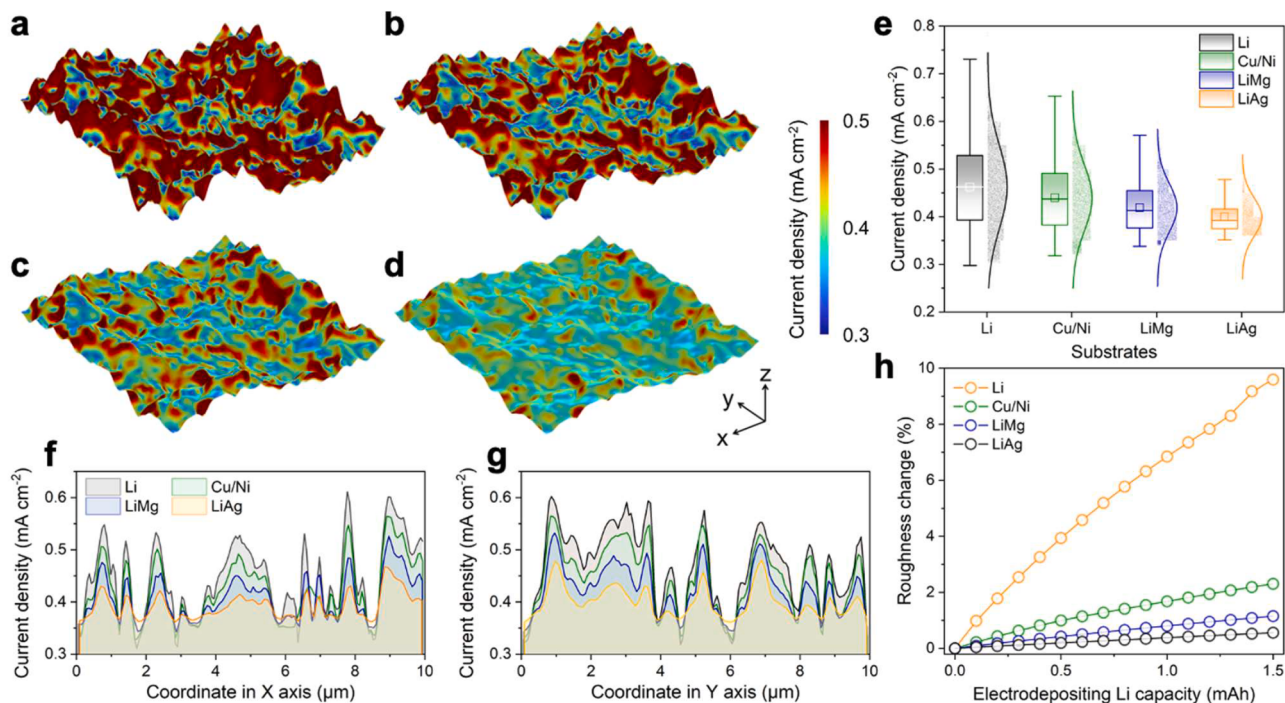


Fig. 6. Morphology evolution of electrodeposited Li on metal substrates with different roughness. Distribution of current density on surface of electrodeposited Li with the roughness of (a) $\text{Ra}=0.38$ (b) $\text{Ra}=0.56$ (c) $\text{Ra}=0.57$ (d) $\text{Ra}=0.95$, which are from the growth of substructures shown in Figure 4. (e) Statistics of current density on different surfaces of electrodeposited Li. Variation of current density (f) along X axis of $y = 5 \mu\text{m}$ and (g) along Y axis of $x = 5 \mu\text{m}$. (h) Roughness evolution of Li surface along the electrodeposition process.

substrate is directly connected to the final morphology of electro-deposited Li. Based on this we suggest that, lowering the energy barrier for self-diffusion on the substrate, using for instance surface modification by lithophilic elements, is a promising direction to enable uniform electrodeposition of Li anodes in rechargeable Li metal batteries. More than that, the Methodological universality of this method can be transplanted to study the electro-crystallization process of other metallic anodes, eg., sodium, potassium, zinc, magnesium, calcium for accelerating the application of next-generation energy storage system.

CRediT authorship contribution statement

XingXing Jiao: Conceptualization, Methodology, Formal analysis, Writing – original draft. **Yongjing Wang:** Software, Resources. **Olesya O. Kapitanova:** Investigation. **Xieyu Xu:** Software, Methodology, Funding acquisition. **Valentyn S. Volkov:** Investigation. **Yangyang Liu:** Conceptualization, Methodology, Visualization, Formal analysis, Writing – review & editing. **Zhongxiao Song:** Resources, Writing – review & editing. **Aleksandar Matic:** Writing – review & editing. **Shizhao Xiong:** Conceptualization, Supervision, Writing – review & editing.

Declaration of Competing Interest

The authors declare that they have no known competing financial interests or personal relationships that could have appeared to influence the work reported in this paper.

Acknowledgments

This work is supported by Batteries Sweden (BASE), the Chalmers Areas of Advance Materials Science and Energy. We thank the National Natural Science Foundation of China (U21B2057, No. 51802256) and China Scholarship Council (No.201908090043) for supporting this work.

Supplementary materials

Supplementary material associated with this article can be found, in the online version, at [doi:10.1016/j.ensm.2023.102916](https://doi.org/10.1016/j.ensm.2023.102916).

References

- [1] D. Lin, Y. Liu, Y. Cui, Nat. Nanotechnol. 12 (2017) 194–206.
- [2] H. Li, Joule 3 (2019) 911–914.
- [3] N. Nitta, F. Wu, J.T. Lee, G. Yushin, Mater. Today 18 (2015) 252–264.
- [4] J. Ma, Y. Li, N.S. Gundish, J.B. Goodenough, Y. Chen, L. Guo, Z. Peng, X. Qi, F. Yang, L. Qie, C.-A. Wang, B. Huang, Z. Huang, L. Chen, D. Su, G. Wang, X. Peng, Z. Chen, J. Yang, S. He, X. Zhang, H. Yu, C. Fu, M. Jiang, W. Deng, C.-F. Sun, Q. Pan, Y. Tang, X. Li, X. Ji, F. Wan, Z. Niu, F. Lian, C. Wang, G.G. Wallace, M. Fan, Q. Meng, S. Xin, Y.-G. Guo, L.-J. Wan, J. Phys. D: Appl. Phys. 54 (2021), 183001.
- [5] B. Liu, J.-G. Zhang, W. Xu, Joule 2 (2018) 833–845.
- [6] P.G. Bruce, S.A. Freunberger, L.J. Hardwick, J.M. Tarascon, Nat. Mater. 11 (2011) 19–29.
- [7] X. Zhang, Y. Yang, Z. Zhou, Chem. Soc. Rev. 49 (2020) 3040–3071.
- [8] J. Zheng, M.S. Kim, Z. Tu, S. Choudhury, T. Tang, L.A. Archer, Chem. Soc. Rev. 49 (2020) 2701–2750.
- [9] F. Sun, C. Yang, I. Manke, L. Chen, S. Dong, Mater. Today 38 (2020) 7–9.
- [10] K.N. Wood, M. Noked, N.P. Dasgupta, ACS Energy Lett. 2 (2017) 664–672.
- [11] J. Xiao, Science 366 (2019) 426–427.
- [12] Z. Wang, Z. Sun, J. Li, Y. Shi, C. Sun, B. An, H.M. Cheng, F. Li, Chem. Soc. Rev. 50 (2021) 3178–3210.
- [13] Y. Liu, X. Xu, M. Sadd, O.O. Kapitanova, V.A. Krivchenko, J. Ban, J. Wang, X. Jiao, Z. Song, J. Song, S. Xiong, A. Matic, Adv. Sci. 8 (2021), 2003301.
- [14] X. Xu, Y. Liu, J.Y. Hwang, O.O. Kapitanova, Z. Song, Y.K. Sun, A. Matic, S. Xiong, Adv. Energy Mater. 10 (2020), 2002390.
- [15] Y.Y. Liu, X.Y. Xu, X.X. Jiao, L.N. Guo, Z.X. Song, S.Z. Xiong, J.X. Song, Chem. Eng. J. 371 (2019) 294–300.
- [16] Y. Gao, T. Rojas, K. Wang, S. Liu, D.W. Wang, T.H. Chen, H.Y. Wang, A.T. Ngo, D. H. Wang, Nat. Energy 5 (2020) 534–542.
- [17] Y. Gao, Z. Yan, J.L. Gray, X. He, D. Wang, T. Chen, Q. Huang, Y.C. Li, H. Wang, S. H. Kim, T.E. Mallouk, D. Wang, Nat. Mater. 18 (2019) 384–389.
- [18] N.W. Li, Y.X. Yin, C.P. Yang, Y.G. Guo, Adv. Mater. 28 (2016) 1853–1858.
- [19] Q. Liu, Y. Liu, X. Jiao, Z. Song, M. Sadd, X. Xu, A. Matic, S. Xiong, J. Song, Energy Storage Mater. 23 (2019) 105–111.
- [20] J.-Y. Hwang, S.-J. Park, C.S. Yoon, Y.-K. Sun, Energy Environ. Sci. 12 (2019) 2174–2184.
- [21] S. Gu, S.W. Zhang, J. Han, Y. Deng, C. Luo, G. Zhou, Y. He, G. Wei, F. Kang, W. Lv, Q.H. Yang, Adv. Funct. Mater. 31 (2021), 2102128.
- [22] R. May, K.J. Fritzsching, D. Livitz, S.R. Denny, L.E. Marbella, Acs Energy Lett. 6 (2021) 1162–1169.
- [23] L. Yangyang, W. Xuyang, X. Xieyu, W. Yongjing, X. Shizhao, S. Zhongxiao, Energy Storage Sci. Tech. 10 (2021) 1261–1272.
- [24] X. Liang, Q. Pang, I.R. Kochetkov, M.S. Sempere, H. Huang, X. Sun, L.F. Nazar, Nat. Energy 2 (2017) 17119.
- [25] S. Xiong, Y. Liu, P. Jankowski, Q. Liu, F. Nitze, K. Xie, J. Song, A. Matic, Adv. Funct. Mater. 30 (2020), 2001444.
- [26] H. Wan, S. Liu, T. Deng, J. Xu, J. Zhang, X. He, X. Ji, X. Yao, C. Wang, ACS Energy Lett. 6 (2021) 862–868.
- [27] Q. Zhou, S. Dong, Z. Lv, G. Xu, L. Huang, Q. Wang, Z. Cui, G. Cui, Adv. Energy Mater. 10 (2019), 1903441.
- [28] Y. Xiao, K. Turcheniuk, A. Narla, A.Y. Song, X. Ren, A. Magasinski, A. Jain, S. Huang, H. Lee, G. Yushin, Nat. Mater. 20 (2021) 984–990.
- [29] A. Masias, J. Marcicki, W.A. Paxton, Acs Energy Lett. 6 (2021) 621–630.
- [30] P. Albertus, S. Babinec, S. Litzelman, A. Newman, Nat. Energy 3 (2017) 16–21.
- [31] J. Xiao, Q.Y. Li, Y.J. Bi, M. Cai, B. Dunn, T. Glossmann, J. Liu, T. Osaka, R. Sugiyra, B.B. Wu, J.H. Yang, J.G. Zhang, M.S. Whittingham, Nat. Energy 5 (2020) 561–568.
- [32] M.S. Kim, S.H.L. Deepika, M.-S. Kim, J.-H. Ryu, K.-R. Lee, L.A. Archer, W.I. Cho, Sci. Adv. 5 (2019) eaax5587.
- [33] B.S. Vishnugop, F. Hao, A. Verma, P.P. Mukherjee, Phys. Chem. Chem. Phys. 22 (2020) 11286–11295.
- [34] D.R. Ely, R.E. García, J. Electrochem. Soc. 160 (2013) A662–A668.
- [35] M. Jäckle, K. Helmbrecht, M. Smits, D. Stottmeister, A. Groß, Energy. Environ. Sci. 11 (2018) 3400–3407.
- [36] W. Liu, P. Liu, D. Mitlin, Chem. Soc. Rev. 49 (2020) 7284–7300.
- [37] K. Yan, Z. Lu, H.-W. Lee, F. Xiong, P.-C. Hsu, Y. Li, J. Zhao, S. Chu, Y. Cui, Nat. Energy 1 (2016) 16010.
- [38] Y. Chen, X. Xu, L. Gao, G. Yu, O.O. Kapitanova, S. Xiong, V.S. Volkov, Z. Song, Y. Liu, Small Methods 6 (2022), e2200113.
- [39] A. Aryanfar, T. Cheng, A.J. Colussi, B.V. Merinov, W.A. Goddard 3rd, M. R. Hoffmann, J. Chem. Phys. 143 (2015), 134701.
- [40] M.E. Hyde, R.G. Compton, J. Electroanal. Chem. 549 (2003) 1–12.
- [41] Y. Liu, S. Xiong, J. Wang, X. Jiao, S. Li, C. Zhang, Z. Song, J. Song, Energy Storage Mater. 19 (2019) 24–30.
- [42] Y.D. Gamburg, Rus. J. Electrochem. 54 (2019) 1298–1300.
- [43] Y. Okajima, Y. Shibuta, T. Suzuki, Comput. Mater. Sci. 50 (2010) 118–124.
- [44] R. Akolkar, J. Power Sources 232 (2013) 23–28.
- [45] Y. Ozhabes, D. Gunceler, T.A. Arias, arXiv:1504.05799v1, (2015).
- [46] J.H. Yang, J.S. Park, J. Kang, S.H. Wei, Phys. Rev. B 91 (2015), 075202. -075201.
- [47] H. Brune, Surf. Sci. Rep. 31 (1998) 121–229.
- [48] A. Einstein, Ann. Phys. 322 (1905) 549–560. German.
- [49] J.R. Espinosa, C. Vega, C. Valeriani, E. Sanz, J. Chem. Phys. 144 (2016), 034501.
- [50] S. Auer, D. Frenkel, J. Chem. Phys. 120 (2004) 3015–3029.
- [51] D. Tewari, P.P. Mukherjee, J. Mater. Chem. A 7 (2019) 4668–4688.
- [52] D. Stauffer, A. Coniglio, D.W. Heermann, Phys. Rev. Lett. 49 (1982) 1299–1302.
- [53] S. Auer, D. Frenkel, Nature 409 (2001) 1020–1023.
- [54] M. Jackle, A. Gross, J. Chem. Phys. 141 (2014), 174710.
- [55] Y. Fan, T. Wang, D. Legut, Q. Zhang, J. Energy Chem. 39 (2019) 160–169.
- [56] D. Gaissmaier, D. Fantauzzi, T. Jacob, J. Chem. Phys. 150 (2019), 041723.
- [57] S.-S. Chi, Y. Liu, W.-L. Song, L.-Z. Fan, Q. Zhang, Adv. Funct. Mater. 27 (2017), 1700348.
- [58] Q. Li, S. Zhu, Y. Lu, Adv. Funct. Mater. 27 (2017), 1606422.
- [59] F. Guo, C. Wu, H. Chen, F. Zhong, X. Ai, H. Yang, J. Qian, Energy Storage Mater. 24 (2020) 635–643.
- [60] Y. Gu, H.Y. Xu, X.G. Zhang, W.W. Wang, J.W. He, S. Tang, J.W. Yan, D.Y. Wu, M. S. Zheng, Q.F. Dong, B.W. Mao, Angew. Chem. Int. Ed. Engl. 58 (2019) 3092–3096.
- [61] K. Huang, Y. Liu, H. Liu, ACS Appl. Mater. Interfaces 11 (2019) 37239–37246.
- [62] S.I. Shah, G. Nandipati, A. Karim, T.S. Rahman, J. Phys. Condens. Matter. 28 (2016), 025001.
- [63] G.C. Sosso, J. Chen, S.J. Cox, M. Fitzner, P. Pedevilla, A. Zen, A. Michaelides, Chem. Rev. 116 (2016) 7078–7116.
- [64] G.M. Torrie, J.P. Valleau, J. Comput. Phys. 23 (1977) 187–199.
- [65] A. Laio, M. Parrinello, Proc. Natl. Acad. Sci. U S A 99 (2002) 12562–12566.
- [66] C. Sendner, A. Gross, J. Chem. Phys. 127 (2007), 014704.
- [67] A. Pei, G. Zheng, F. Shi, Y. Li, Y. Cui, Nano Lett. 17 (2017) 1132–1139.
- [68] Y. Sun, H. Song, F. Zhang, L. Yang, Z. Ye, M.I. Mendelev, C.Z. Wang, K.M. Ho, Phys. Rev. Lett. 120 (2018), 085703.
- [69] A. Lyon, Brit. J. Phil. Sci. 65 (2014) 621–649.
- [70] S. Wolfram, Rev. Mod. Phys. 55 (1983) 601–644.